


## Measurement backaction control of quantum dissipation in a nonlinear cavity-based Duffing oscillator

Yueheng Shi, Sacha Greenfield,<sup>\*</sup> and Arjendu K. Pattanayak<sup>†</sup>

*Department of Physics and Astronomy, Carleton College, 1 North College Street, Northfield, Minnesota 55057, USA*

 (Received 21 December 2020; revised 21 April 2021; accepted 22 April 2021; published 20 May 2021)

Quantum backaction from weak measurement affects the behavior of quantum systems. We consider a nonlinear driven Duffing oscillator system implementation in a nonlinear optical cavity, and we show that the choice of phase setting  $\phi$  for a laser used in measurement can change the dissipation for the spread variables of the quantum state. This can considerably increase the energy absorbed via the energy channel of the spread variables and enhance quantum effects. This suggests novel applications to quantum control, as we demonstrate, including an example in which the energy in the spread variables allows for a dynamical tunneling between energetically separated dynamical steady-states.

DOI: [10.1103/PhysRevA.103.052212](https://doi.org/10.1103/PhysRevA.103.052212)

### I. INTRODUCTION

We are at the early stages of a “second quantum revolution” [1] with rapid advances exploiting desirable and potentially powerful properties such as entanglement and coherence that promise even more than what the last 100 years have provided by way of semiconductor technology, lasers, and chemical and medical imaging such as in spectroscopy and NMR. Quantum properties are, however, sensitive to interactions with an environment (which leads to decoherence) and in “state collapse” during measurement, both considered troubling for engineering purposes. However, advances in theory and experiment have led us to understand that it is possible to account for changes induced both by the environment and by the measurement backaction, and that these quantum effects can be exploited in a manner not possible in classical control [2,3]. If the measurement is adaptive (where system parameters are changed in response to measurement results), these effects can be used to improve phase estimation [4], in quantum state preparation [5], and to improve quantum measurements [6]; other work uses measurement for entanglement generation [7], state stabilization [8], and other innovative techniques relevant to quantum foundations and engineering. Recently, proposals have been made for observing such phenomena in nonlinear nanoelectromechanical systems (NEMS) oscillators [9] being driven by a sinusoidal external source and subject to environmental decoherence and dissipation. Newer proposals consider a situation in which the optical signal reflecting off the NEMS oscillator is interfered with a local oscillator (LO) laser in what is termed a homodyne measurement, described more below. In particular, the “angle”  $\phi$  of a phase setting for the LO laser used in measurement was shown to considerably affect the dynamics of a bistable nonlinear quantum oscillator,

allowing  $\phi$  settings to induce or suppress quantum trajectory chaos and dynamical complexity as measured by a quantum Lyapunov exponent [10].

In this paper, we extend this work further. First, we propose a different experimental implementation for such a continuously monitored driven nonlinear quantum oscillator, in this case based on the same homodyne measurement but with the nonlinear oscillator realized in a nonlinear optical cavity. We show how parameter choices for this system could reproduce the appropriate trajectory equations for a quantum Duffing oscillator model. Next, we present an analysis of the measurement effect of  $\phi$  within a semiclassical approximation valid for sufficiently strong coupling to the environment. In this regime, due to dissipative localization, the quantum state trajectory dynamics can be accurately approximated by a Gaussian quantum wave packet. In the absence of dissipation (and measurement), a representation [11] exists of the semiclassical system as two oscillators with an effective Hamiltonian  $H(x, p, \chi, \Pi) = p^2/2 + \Pi^2/2 + U(x, \chi)$  such that the dynamics evolve in a two-dimensional potential  $U(x, \chi)$ . One of these oscillators is associated with the quantum centroid  $(x, p)$  and the other with the spread variables  $(\chi, \Pi)$ —defined more carefully below—of the quantum state. As we show, the effect of the environment and measurement backaction can be understood as generalized dissipation  $\vec{F}$  and noise  $\vec{N}$  for these coupled oscillators, where both forces have a complicated  $\phi$  dependence. Interestingly,  $\vec{N}$  couples exclusively to the  $(x, p)$  oscillator, while the  $\phi$ -dependent part of  $\vec{F}$  couples only to the  $(\chi, \Pi)$  oscillator. The noise force typically does not alter quantum trajectories significantly. The generalized dissipation force, however, provides a novel opportunity to use the backaction effect of changing the measurement angle to control wave-function dynamics via the behavior of the quantum spread variables. In particular, the semiclassical analysis clarifies how changing  $\phi$  affects the nonclassical contributions to the Hamiltonian, which changes global system dynamics and energy. These changes in the system energy map onto changes in accessible  $U(x, \chi)$

<sup>\*</sup>Present address: Department of Physics, University of Southern California, Los Angeles 90089, USA.

<sup>†</sup>arjendu@carleton.edu

regions, which explains the observed  $\phi$ -dependent dynamics previously reported [10,12,13], all induced entirely by measurement backaction.

Based on this intuition, we deduce adaptive-choice  $\phi$  protocols that extremize specific energy channels for dissipation. Our simulation results show that compared to fixed- $\phi$  responses, these adaptive protocols achieve dramatic (many orders of magnitude) increases in the energy range of the  $\chi$ ,  $\Pi$  spread oscillator, thus considerably changing the coupled oscillator dynamics compared to systems of the same size not subject to measurement feedback control. We show how novel dynamics can be induced in this manner, including an example where the quantum spread variables absorb energy that is instrumental in the system transitioning between two energetically separated dynamical steady-states. Using the size of the nonclassical contributions to the overall system energy as a measure of nonclassicality, we see that—remarkably—the postprocessing  $\phi$ -dependence proposed here can alter environmental effects enough to be substantially more important than length scale in determining the degree of nonclassicality. Thus, this novel mechanism using backaction via the spread variables offers a promising avenue for exploring novel quantum phenomena.

In Sec. II we present the background theory and experimental proposal. In Sec. III we introduce the semiclassical coupled oscillator. We examine the energy dynamics analytically and show how the  $\phi$ -dependence may be understood via its effects on dissipation into the environment from the quantum system. We also propose adaptive control protocols. In Sec. IV we present examples of the various interesting results we have seen in our simulations, focusing on a novel transition from chaotic to regular behavior involving abrupt energy exchange between the classical and spread variables. Finally, we close in Sec. V with a short discussion of these results.

## II. CONTINUOUSLY MONITORED DUFFING OSCILLATOR IN A NONLINEAR OPTICAL CAVITY

The dynamical system we study is the open quantum Duffing oscillator, a paradigmatic model to study quantum to classical transition for chaotic systems [14]. The Newtonian limit is a unit mass in a double-well potential with dissipation  $\Gamma$ , sinusoidal driving amplitude  $g$ , frequency  $\omega$ , and dimensionless length scale  $\beta$ ,

$$\ddot{x} + 2\Gamma\dot{x} + \beta^2 x^3 - x = \frac{g}{\beta} \cos(\Omega t). \quad (1)$$

This renders time dimensionless as well. The quantum version is described using a quantum trajectory formalism adapted to include measurements where the stochastic evolution of a single pure quantum system  $|\psi\rangle$  under continuous measurement is considered. We start with the Hamiltonian  $H = H_D + H_R$  [10,12,13,15–18],

$$\hat{H} = \frac{1}{2}\hat{P}^2 + \frac{\beta^2}{4}\hat{Q}^4 - \frac{1}{2}\hat{Q}^2 + \frac{\Gamma}{2}(\hat{Q}\hat{P} + \hat{P}\hat{Q}) - \frac{g}{\beta}\hat{Q} \cos(\Omega t), \quad (2)$$

where we continue to work with dimensionless variables including time, which effectively sets  $\hbar = 1$  as well. We note

that the Hamiltonian above is the sum  $\hat{H} = \hat{H}_R + \hat{H}_D$ , where

$$\hat{H}_R = \frac{\Gamma}{2}(\hat{Q}\hat{P} + \hat{P}\hat{Q}) \quad (3)$$

is added to the quantized version  $\hat{H}_D$  of the classical Hamiltonian

$$H_D = \frac{p^2}{2} - \frac{x^2}{2} + \frac{\beta^2 x^4}{4} + \frac{gx}{\beta} \cos(\Omega t) \quad (4)$$

to account for the fact that without this term, and with the chosen Lindblad operator below, the quantum dissipation would be symmetric in  $\hat{Q}$  and  $\hat{P}$ . This is contrary to the classical limit Eq. (1) where dissipation appears only via the momentum variable; adding this term yields the correct classical limit. That limit itself is formally obtained for the open quantum Duffing system by changing the dimensionless effective Planck's constant  $\beta$  [15–18] where increasing  $\beta$  describes smaller systems and  $\beta \rightarrow 0$  is the classical limit. Thus, by varying  $\beta$ , we can describe the system's transition from classical to quantum length scales.

Environmental effects enter via a coupling of the system with a zero-temperature Markovian bath corresponding to  $\hat{a} = (\hat{Q} + i\hat{P})/\sqrt{2}$  in the decoherence superoperator formalism [19,20], as shown in Eq. (5) below. This dissipative quantum channel is weakly and continuously monitored, such that the system state evolves conditioned on the measurement outcomes via the Ito stochastic equation [21,22]

$$|d\psi\rangle = \left( -\frac{i}{\hbar}\hat{H} + \langle\hat{L}^\dagger\rangle\hat{L} - \frac{\hat{L}^\dagger\hat{L}}{2} - \frac{\langle\hat{L}^\dagger\rangle\langle\hat{L}\rangle}{2} \right) |\psi\rangle dt + (\hat{L} - \langle\hat{L}\rangle) |\psi\rangle d\xi. \quad (5)$$

Here,  $\hat{L} = \sqrt{2\Gamma}\hat{a}$  represents the dissipative environment interacting with strength  $\Gamma$ , and  $\hat{H} = \hat{H}_D + \hat{H}_R$ . The random or noisy dynamics induced by the measurement is represented as the complex-valued Wiener process,  $d\xi$ , with the mean  $M$  over realizations constrained as  $M(d\xi) = 0$ ,  $M(d\xi d\xi) = u$ ,  $M(d\xi d\xi^*) = dt$ . Further, as noted in [14], since the variance of stochastic variables such as  $M(d\xi)^2 - (d\xi)^2$  is of order  $dt^2$ , it and similar higher-order terms vanish, allowing us to also write [21]  $d\xi d\xi^* = dt$  and  $d\xi d\xi = u dt$ .

Here the complex parameter  $u = |u|e^{-2i\phi}$  must satisfy the condition  $|u| \leq 1$  [21,22] and is related to properties of the measurement setup, as we discuss in detail below. The situation  $u = 0$  corresponds to the unmonitored environment. We focus in our work on the properties of pure state evolution of conditioned trajectories (also discussed more carefully below), and hence we assume an idealized, lossless detection, which ensures that the quantum state remains pure in spite of measurement, and Eq. (5) applies [21]. It has previously been shown [9] that nanoelectromechanical systems are well described by this model, and current experiments are within the range of the parameters used; however, it is difficult to set up an appropriate weak-measurement scheme to achieve the quantum backaction effects being considered.

In this context, optical nonlinear oscillators may prove more viable. Among the previously proposed optical nonlinear oscillators, the nonlinearity is introduced through the Kerr effect induced by the third-order electric susceptibility  $\chi^{(3)}$  [23–26]. Here we adapt this to propose a nonlinear optical

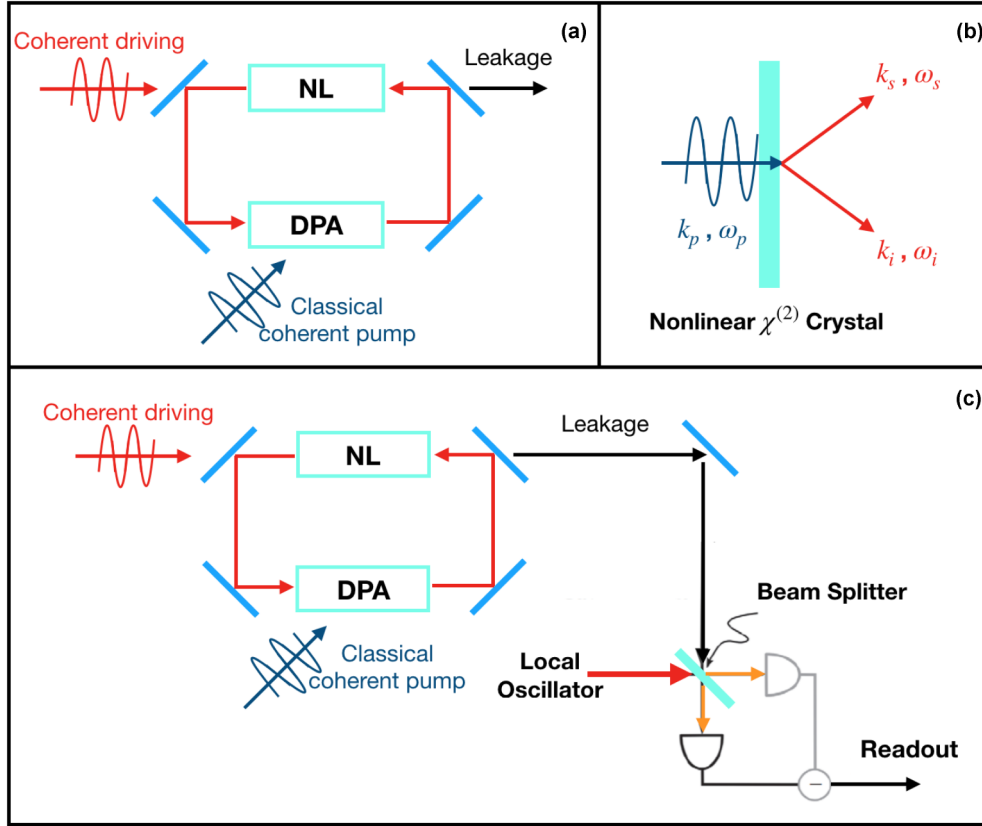


FIG. 1. The schematic for the nonlinear cavity-based quantum Duffing oscillator. (a) The nonlinear cavity consists of a nonlinear medium (NL) with susceptibilities  $\chi^{(1)} < 0$  and  $\chi^{(3)} > 0$  driven by a coherent laser (red) and a degenerate parametric amplifier (teal, DPA). (b) The DPA is pumped by a classical coherent field. (c) Leakage from the nonlinear cavity is mixed with a local oscillator (LO), coherent with the classical coherent field in (b), to perform a homodyne detection.

cavity-based quantum Duffing oscillator with a double-well potential through a combination of  $\chi^{(1)}$  and  $\chi^{(3)}$  susceptibilities. The schematic of the proposed system is shown in Fig. 1(a) based on the setup employed in Ref. [23] to investigate the emergence of quantum chaos. A coherent laser drives an optical cavity through one mirror and there is light leaking out of the mirror on the other side of the cavity. Inside the cavity, the laser drives the interaction of the light field with a nonlinear medium (NL) and a degenerate parametric amplifier (DPA) pumped by a classical light field. Here we assume the cavity to be operating as a single-mode cavity. In the following, we discuss how certain choices of parameters in the model could reproduce the Hamiltonian in Eq. (2) and the measurement scheme which corresponds to the SSE in Eq. (5).

In Ref. [23], the nonlinear oscillator in Fig. 1(a) is treated as a Kerr medium with a fourth-order interaction that has the Hamiltonian  $H_{\text{Kerr}} = \hat{a}^\dagger \hat{a}^\dagger \hat{a} \hat{a}$  under the rotating wave approximation (RWA) with the possibility for a bistable potential. To create a double-well potential similar to the Duffing oscillator model, we rederive the Hamiltonian for this specific nonlinear system by following the same approach in Ref. [24]. For a light field interacting with a nonlinear dielectric medium, the polarization  $P$  of the medium has a nonlinear response that can be described by expanding up to the third order in the electric field  $E$  and the susceptibility tensors as

$$P = \chi^{(1)} \cdot E + \chi^{(2)} \cdot EE + \chi^{(3)} \cdot EEE, \quad (6)$$

where  $\chi^{(n)}$  is the  $(n+1)$ th rank susceptibility tensor, and  $\cdot$  represents the appropriate tensor contraction. Through the standard vector potential of electromagnetic fields, the Hamiltonian of this field in the nonlinear medium can be obtained as

$$H =: \int d^3r \left\{ \frac{|B|^2}{2\epsilon_0} + E \left[ \frac{(\epsilon_0 + \chi^{(1)})}{2} E + \frac{\chi^{(2)}}{3} EE + \frac{\chi^{(3)}}{4} EEE \right] \right\} :, \quad (7)$$

where we have taken the contribution of the magnetic field as a constant since the dielectric medium only interacts with the electric field, and  $::$  denotes normal ordering. To quantize the Hamiltonian, we proceed as usual and substitute the electric field with the normal-mode expanded field operator as

$$E = \left( \frac{\hbar\omega}{2\epsilon_0} \right)^{1/2} (\hat{a}u(r) + \hat{a}^\dagger u^*(r)), \quad (8)$$

where  $u(r)$  is the transverse mode of the field, and  $\omega$  is the frequency of the light field. We choose  $u(r)$  such that  $u(r) = u^*(r)$ , and we constrain it to satisfy

$$\int [1 + \chi^{(1)}(r)/\epsilon_0] |u(r)|^2 d^3r = -1, \quad (9)$$

where we have assumed  $\chi^{(1)}$  to be negative. Then if we neglect the term in  $\chi^{(2)}$  due to a lack of phase-matching, we

arrive at the Hamiltonian

$$\hat{H}_{\text{Kerr}} = -\hbar\chi'(\hat{a} + \hat{a}^\dagger)^2 + \hbar^2\chi''(\hat{a} + \hat{a}^\dagger)^4, \quad (10)$$

where  $\chi' = \frac{1}{4}\omega$  and  $\chi'' = \frac{\hbar}{4}(\frac{\omega}{2\epsilon_0})^2 \int |u(r)|^4 \chi^{(3)}(r) dr^3$ . By defining the quadratures as  $\hat{Q} = (\hat{a}^\dagger + \hat{a})/2$  and  $\hat{P} = i(\hat{a}^\dagger - \hat{a})/2$ , we can rewrite Eq. (10) as  $\hat{H}_{\text{Kerr}} \propto -a\hat{Q}^2 + b\hat{Q}^4$ .  $\hat{Q}$  and  $\hat{P}$  are analogous to the position and momentum observable of a harmonic oscillator, respectively. It is clear that the classical version of Eq. (10) represents the double-well form of the anharmonic potential ( $-ax^2 + bx^4$ ), as in  $\hat{H}_D$  of the Duffing model.

Next, to obtain the  $\hat{H}_R$  terms described above, we introduce the DPA in Fig. 1(a), which refers to a spontaneous parametric downconversion process, as shown in Fig. 1(b). The parametric amplifier is described by the Hamiltonian [27,28]

$$\hat{H}_{\text{DPA}} = \hbar\kappa(\hat{a}_i^\dagger \hat{a}_s^\dagger \hat{a}_p e^{-i\Delta\vec{k}\cdot\vec{r} + i\Delta\omega t} + \hat{a}_i \hat{a}_s \hat{a}_p^\dagger e^{i\Delta\vec{k}\cdot\vec{r} - i\Delta\omega t}), \quad (11)$$

where  $\vec{k}_m$  and  $\omega_m$  are the photon's wave vectors and frequencies, respectively, and  $\Delta\vec{k} = \vec{k}_p - \vec{k}_i - \vec{k}_s$ ,  $\Delta\omega = \omega_p - \omega_i - \omega_s$ . The first term in the Hamiltonian describes the annihilation of the incident pump photon ( $a_p$ ) and the creation of one idler photon ( $a_i$ ) and one signal photon ( $a_s$ ); the second term describes the reverse process of creation. The interaction strength  $\kappa$  is proportional to the susceptibility of the medium  $\chi^{(2)}$ . Now for the degenerate case, the idler and signal photons are of the same mode, i.e.,  $\hat{a}_s = \hat{a}_p = \hat{a}$ , and the perfect phase-matching condition— $\vec{k}_p = \vec{k}_i + \vec{k}_s$  and  $\omega_p = \omega_i + \omega_s$ —is assumed to conserve the momentum and energy in the system. Moreover, the pump field is considered to be an intense coherent beam that can be approximated as a coherent classical field. Therefore, we can take  $\hat{a}_p \rightarrow |\alpha|e^{-i\theta}(\hat{a}_p^\dagger \rightarrow |\alpha|e^{i\theta})$ , where  $\alpha$  and  $\theta$  correspond to the amplitude and the phase of the pump field. For the sake of simplicity, we take  $|\alpha| = 1$  and  $\theta = \pi/2$  absorbing the specifics of  $|\alpha|$  into a redefinition of  $\kappa$ . Eventually the Hamiltonian of the degenerate parametric amplifier becomes

$$\hat{H}_{\text{DPA}} = \hbar\kappa(i\hat{a}^{\dagger 2} - i\hat{a}^2), \quad (12)$$

which is similar to that in Ref. [23] except that we assume the phase-matching condition to be perfect while Milburn and Holmes specify the relationship between the pump frequency and the fundamental cavity frequency.

Following an approach similar to Ref. [24], the combined system shown in Fig. 1(a) is now described by the total Hamiltonian

$$\hat{H} = \hat{H}_{\text{cav}} + \hat{H}_{\text{DPA}} + \hat{H}_{\text{Kerr}} + \hat{H}_{\text{drive}}, \quad (13a)$$

$$\hat{H}_{\text{cav}} = \hbar\omega_c \hat{a}^\dagger \hat{a}, \quad (13b)$$

$$\hat{H}_{\text{drive}} = \hbar(\epsilon \hat{a}^\dagger e^{-i\omega_L t} + \epsilon^* \hat{a} e^{i\omega_L t}), \quad (13c)$$

with  $H_{\text{Kerr}}$ ,  $H_{\text{DPA}}$  as in Eqs. (10) and (12) and where  $\hat{H}_{\text{cav}}$  is the Hamiltonian for the single-mode cavity and  $\hat{H}_{\text{drive}}$  is the coherent driving input into the cavity with frequency  $\omega_L$ . The combined Hamiltonian can be rewritten in terms of  $\hat{Q}$  and  $\hat{P}$

as

$$\hat{H} = \hat{H}_{\text{cav}} + \hat{H}_{\text{DPA}} + \hat{H}_{\text{Kerr}} + \hat{H}_{\text{drive}}, \quad (14a)$$

$$\hat{H}_{\text{cav}} + \hat{H}_{\text{Kerr}} = -\hbar\omega_c \hat{Q}^2 + \hbar\omega_c \hat{P}^2 + \frac{\hbar^2\chi''\hat{Q}^4}{16}, \quad (14b)$$

$$\hat{H}_{\text{DPA}} = 4\hbar\kappa(\hat{P}\hat{Q} + \hat{Q}\hat{P}), \quad (14c)$$

$$\hat{H}_{\text{drive}} = \hbar\frac{\epsilon}{2}\hat{Q}\cos(\omega_L t), \quad (14d)$$

where we have chosen  $\chi'$  and  $\omega_c$  to satisfy  $\omega_c = \chi'/8$  and  $\epsilon$  to be real. By defining  $\beta = \sqrt{\frac{\chi''}{8\omega_c}}$ ,  $\Gamma = \frac{4\kappa}{\omega_c}$ , and  $g = \frac{\epsilon}{8\omega_c}\sqrt{\frac{\chi''}{2\omega_c}}$ , and doing the transformation  $\hat{Q} \rightarrow \frac{\hat{Q}}{\sqrt{\hbar\omega_c}}$  and  $\hat{P} \rightarrow \frac{\hat{P}}{\sqrt{\hbar\omega_c}}$ , we can rewrite the above Hamiltonian in the dimensionless  $\beta$ -dependent form

$$\hat{H} = \hat{H}_D + \hat{H}_R, \quad (15a)$$

$$\hat{H}_D = \frac{1}{2}\hat{P}^2 + \frac{\beta^2}{4}\hat{Q}^4 - \frac{1}{2}\hat{Q}^2 - \frac{g}{\beta}\hat{Q}\cos(\omega t), \quad (15b)$$

$$\hat{H}_R = \frac{\Gamma}{2}(\hat{Q}\hat{P} + \hat{P}\hat{Q}), \quad (15c)$$

which is precisely the Hamiltonian from Eq. 2. It is worth remarking that  $H_{\text{DPA}}$  in terms of annihilation and creation operators in Eq. (15) matches the general form of squeezing operator suggested in Ref. [29]. However, when this Hamiltonian is written in the quadrature operator form, we see that this is the Hamiltonian term we added to our quantum Duffing oscillator to reproduce the classical dissipation. This connects the generation of squeezed states with the limiting classical dissipation model in an interesting way, in that in the absence of this term, the classical dissipation would be symmetric in  $\hat{P}$ ,  $\hat{Q}$ .

Finally, we implement a conventional homodyne measurement scheme to weakly and continuously measure the cavity, as shown in Fig. 1(c). In this scheme, the local oscillator (LO) is a laser beam coherent with the classical pump to the DPA, with a certain phase  $\phi$  known as the measurement angle. As a result, the leakage from the cavity interferes coherently with the LO, providing information about the cavity state depending on the choice of  $\phi$ . For example, setting  $\phi = 0$  corresponds to weakly measuring  $\hat{Q}$ , leading to measurement backaction in  $\langle\hat{Q}\rangle$ ; similarly,  $\phi = \pi/2$  corresponds to weakly measuring  $\hat{P}$ , generating measurement backaction in  $\langle\hat{P}\rangle$ . Intermediate settings lead to partial backaction in both quadratures. Thus, by (adaptively) changing  $\phi$ , we can control the system dynamics via measurement backaction, a uniquely quantum pathway to control.

We note again that we assume a lossless detection; in other words, 100% of the leakage from the cavity arrives at the beamsplitter. This allows us to describe the process using the stochastic Schrodinger equation [SSE, Eq. (5)] rather than the stochastic master equation (SME), greatly reducing the computational complexity of the problem [21]. We also take  $|u| = 1$  [12,21], with  $\phi$  being the LO phase, as described. In this case, the noise can be written as  $d\xi = e^{-i\phi}dW$ , where  $dW$  is a real Wiener process.

Here, a few comments on interpretation are appropriate. Since the system is being modeled as being weakly and continuously monitored, it is understood that the state undergoes



a partial collapse at each time step based on the measurement record, which is inherently random. In other words, we are working with quantum “trajectories.” However, unlike the quantum state dynamics (QSD) formalism [14], in which trajectories are arbitrary unravelings of the master equation such that in principle a physical meaning only exists for the ensemble average, here the inclusion of measurement yields physically meaningful trajectories. Specifically, the quantum state evolves (is updated) based on the Hamiltonian as well as the measurement record, which corresponds to a particular readout from the detectors in Fig. 1(c). In the laboratory, such a “conditioned” quantum trajectory represents the best estimate of an *actual* quantum state of the cavity, which could be validated via tomography, as has been done with quantum trajectories in superconducting transmon qubits [30,31]. Thus, the effects observed by changing  $\phi$  disappear in the ensemble average (as we have verified; see Appendix C), but they also exist for the conditioned state.

Finally, note that by deriving our Hamiltonian Eq. (15) from the experimental setup of Fig. 1, we have shown that our model Hamiltonian can be replicated experimentally. Before we proceed to the analysis and results below, we note that this is only a proof-of-principle proposal, since our model does not yet account for several experimental realities including lossy detection, the details of the conditioning of the state evolution based on the measurement record, nor inclusion of the time-delay implicit in control implementations. We briefly discuss future work that could account for these experimental realities in Sec. V.

To gain intuition for the measurement backaction forces, focusing on the effects of changing  $\phi$  adaptively, we now turn to a semiclassical analysis of the system.

### III. SEMICLASSICAL ANALYSIS AND CONTROL PROTOCOL

Equation (5) represents our best model for the evolution of the quantum state of the Duffing oscillator open to the environment and subject to continuous weak monitoring. However, it is not easy to get an intuitive grasp of the physics of the system from these equations, and particularly not into the effects of the measurement phase on the system dynamics. As has been previously established, a semiclassical analysis proves very useful to improve the computational efficiency as well as provide physical insights [17,18,32] to understand this nonlinear system. Here, using a Gaussian approximation that is valid when the quantum state is sufficiently localized by the dissipation, the full quantum dynamics are expressed in terms of those of the centroid variables  $\langle \hat{Q} \rangle = x$ ,  $\langle \hat{P} \rangle = p$ , coupled to higher-order moments of the distribution; this otherwise infinite hierarchy becomes finite when these higher-order moments are computed using the approximation of a Gaussian wave function [11]. For the optical system this is easily interpreted, since  $x$  and  $p$  represent the expectation value of the two quadratures that are output from the nonlinear cavity. In Ref. [33] it has been demonstrated that this semiclassical approximation provides a qualitatively correct result for a quantum optical Kerr model at the bistable regime. Further, the inclusion of the dissipative effects only serves to further

localize the wave function, reinforcing the validity of this approximation [18].

With these justifications, and a derivation more carefully detailed below (see Appendix B), in this limit  $|\psi(t)\rangle$  is accurately and completely described by its parameters, which are represented by the the 4D phase-space vector  $\vec{X} = (x, p, \chi, \Pi)$  with dynamics given by

$$dx = p dt + \sqrt{\Gamma} N_x(\phi, \chi, \Pi) dW, \quad (16a)$$

$$dp = \left( x - \beta^2 x^3 + \frac{g}{\beta} \cos \omega t + \Gamma F_p - 3x\beta^2 \chi^2 \right) dt + \sqrt{\Gamma} N_p(\phi, \chi, \Pi) dW, \quad (16b)$$

$$d\chi = \Pi dt + \Gamma F_\chi(\phi, \chi, \Pi) dt, \quad (16c)$$

$$d\Pi = \chi [1 - 3\beta^2(x^2 + \chi^2)] dt + \frac{1}{4\chi^3} dt + \Gamma F_\Pi(\phi, \chi, \Pi) dt. \quad (16d)$$

Here we introduce the variables  $\chi, \Pi$ , which are defined in terms of the moments of the wave function (see Appendix B for details), with  $\Delta \hat{u} = \hat{u} - \langle \hat{u} \rangle$  for an arbitrary operator, as

$$\chi^2 = \langle \Delta \hat{Q}^2 \rangle, \quad (17a)$$

$$\chi \Pi = \langle \Delta \hat{Q} \Delta \hat{P} + \Delta \hat{P} \Delta \hat{Q} \rangle. \quad (17b)$$

The Gaussian form maintains the relationship

$$\langle \Delta \hat{P}^2 \rangle = \frac{\hbar^2 + \langle \Delta \hat{Q} \Delta \hat{P} + \Delta \hat{P} \Delta \hat{Q} \rangle^2}{4 \langle \Delta \hat{Q}^2 \rangle} \quad (18)$$

such that the three second-moment variables describing the Gaussian reduce to two; this minimum uncertainty condition turns out to be [34] a stable fixed point of the dissipative model.

We also introduce compact notation describing the stochastic forces  $\sqrt{\Gamma} \vec{N} dW$ , where  $\vec{N} = (N_x, N_p, 0, 0)$ , and dissipations  $\Gamma \vec{F}$ , where  $\vec{F} = (F_x, F_p, F_\chi, F_\Pi)$ . These terms encapsulate the effects of continuous monitoring of the cavity:  $\vec{N}$  describes the amplitude and quadrature of the backaction, while  $\vec{F}$  describes the corresponding dissipative terms, as required by the fluctuation-dissipation theorem. The forces  $\vec{N}$  are given by

$$N_x = 2 \left( \chi^2 - \frac{1}{2} \right) \cos(\phi) + 2\chi \Pi \sin(\phi), \quad (19a)$$

$$N_p = 2 \left( \frac{1}{4\chi^2} + \Pi^2 - \frac{1}{2} \right) \sin(\phi) + 2\chi \Pi \cos(\phi), \quad (19b)$$

while the dissipation  $\vec{F}$  has centroid damping  $F_x=0, F_p=-2p$  and spread damping

$$F_\chi = \left[ \chi - \chi^3 + \chi \Pi^2 - \frac{1}{4\chi} \right] \cos(2\phi) - \Pi [-1 + 2\chi^2] \times \sin(2\phi) + \chi - \chi^3 - \chi \Pi^2 + \frac{1}{4\chi}, \quad (20a)$$

$$F_\Pi = \left[ \Pi^3 - \Pi + \frac{3\Pi}{4\chi^2} - \Pi \chi^2 \right] \cos(2\phi) - \left[ -\frac{1}{4\chi^3} + \frac{1}{\chi} - \chi + 2\chi \Pi^2 \right] \sin(2\phi) + \left( -\Pi^3 - \Pi - \frac{3\Pi}{4\chi^2} - \Pi \chi^2 \right). \quad (20b)$$

More details for these equations can be found in the Appendix. Most importantly, these equations demonstrate that it is possible to affect the dynamics of the wave-packet centroid  $(x, p)$  by affecting the dynamics of the wave-packet spread  $(\chi, \Pi)$  via the choice of  $\phi$ . This coupling between the centroid and the spread variables exists *only* for nonlinear Hamiltonians. The effects of this force as a dissipation effect for the spread variables are best seen by considering the impact on the various energy terms as follows. Under the semiclassical approximation, the Hamiltonian in Eq. (15) at  $\Gamma = 0$  becomes

$$H(x, p, \chi, \Pi) = \frac{1}{2}p^2 + \frac{1}{2}\Pi^2 + \frac{g}{\beta}x \cos \omega t + U_1(x) + U_2(\chi) + U_{12}(x, \chi), \quad (21a)$$

$$U_1(x) = -\frac{1}{2}x^2 + \frac{1}{4}\beta^2 x^4, \quad (21b)$$

$$U_2(\chi) = \frac{3}{4}\beta^2 \chi^4 - \frac{1}{2}\chi^2 + \frac{1}{8\chi^2}, \quad (21c)$$

$$U_{12}(x, \chi) = \frac{3}{2}\beta^2 x^2 \chi^2. \quad (21d)$$

The rate of change of the energy in the system is easily shown to be

$$\begin{aligned} \frac{dH}{dt} &= \frac{g}{\beta} \cos(\omega t)p - 2\Gamma p^2 + \Gamma F_{\Pi} \Pi \\ &+ \Gamma F_{\chi} \left( -\frac{1}{4\chi^3} - \chi + x^2 \beta^2 \chi + 3\beta^2 \chi^3 \right). \end{aligned} \quad (22)$$

It is then straightforward to observe that the first two terms of  $dH/dt$  arise from the classical driving and classical dissipation, i.e., terms associated with  $(p, \dot{p})$ . The rest of the  $dH/dt$  terms are all dependent on the purely quantal  $\chi$ - $\Pi$  terms. In other words, the latter change of energy is due to the “quantum” dissipation arising from the coupling of the spread variables to the environment and the measurement. That is,  $dH/dt$  may be appropriately rewritten in terms of the classical and quantum effects as

$$\frac{dH}{dt} = \left. \frac{dH}{dt} \right|_{cl} + \left. \frac{dH}{dt} \right|_q, \quad (23a)$$

$$\left. \frac{dH}{dt} \right|_{cl} = \frac{g}{\beta} \cos(\omega t)p - 2\Gamma p^2, \quad (23b)$$

$$\begin{aligned} \left. \frac{dH}{dt} \right|_q &= \Gamma F_{\Pi} \Pi + \Gamma F_{\chi} \left( -\frac{1}{4\chi^3} - \chi + 3x^2 \beta^2 \chi + 3\beta^2 \chi^3 \right) \\ &= \nabla_{\chi, \Pi} H \cdot (F_{\chi}, F_{\Pi}), \end{aligned} \quad (23c)$$

where the last equation reminds us that changes of energy arise only from the directions perpendicular to a Hamiltonian surface.

To understand the dynamical effects of the dissipation force  $\vec{F} = (F_{\chi}, F_{\Pi})$ , note that we can rewrite Eqs. (20) as

$$\begin{aligned} \vec{F} &= \vec{F}_0 + \vec{F}_{\phi} \\ &= \vec{F}_0 + \vec{F}_c \cos 2\phi + \vec{F}_s \sin 2\phi, \end{aligned} \quad (24)$$

where  $\vec{F}_0, \vec{F}_c, \vec{F}_s, \vec{F}_{\phi}$  are defined by comparing Eqs. (20) and (24). These three components of  $\vec{F}$  are plotted in Fig. 2; note that  $\vec{F}$  at a general  $\phi$  is a weighted superposition of

$\vec{F}_c, \vec{F}_s$ , and  $\vec{F}_0$ . For example, at  $\phi = 0$ ,  $\vec{F} = \vec{F}_0 + \vec{F}_c$ , and at  $\phi = \pi/2$ ,  $\vec{F} = \vec{F}_0 - \vec{F}_c$ . In the latter case,  $\vec{F}_0$  and  $\vec{F}_c$ , both along the  $\Pi = 0$  axis, act in opposite directions and tend to cancel out, while in the former case they add up, forcing the system toward small values of  $\chi$ . Thus, we can predict that when  $\phi$  is chosen such that  $\vec{F}_{\phi}$  points generally “outward,” the dissipation action of the environment on  $\chi$  is decreased and the nonclassical effects, such as interwell transitions, are enhanced. In contrast, when  $\vec{F}_{\phi}$  points “inward,” the dissipative force suppresses higher  $\chi$  values and arguably makes the wave packet more localized, hence rendering the system even more “classical.”

This analysis immediately suggests a direction for control protocols to exploit this situation: We can vary the measurement angle  $\phi$  chosen so as to decrease the dissipation effect (effectively always pushing the dynamics “outward” toward larger  $\chi, \Pi$ ), which increases the nonclassical  $U_{12}$  term in the full Hamiltonian. It can be observed in Eq. (21) that when  $\chi$  is larger,  $U_{12}$  is amplified in the same way as increasing  $\beta$ , which effectively makes the system more “quantum,” while simultaneously increasing the total energy. As before, the source of the system’s energy is the driving  $(g/\beta) \cos \omega t$ ; adapting  $\phi$  has simply altered system dynamics to make a new energetic regime accessible. In other words, the adaptive measurement scheme alters the flow of energy through the system, so that the energy normally dissipated out into the environment is now stored in the oscillator dynamics, including the  $(\chi, \Pi)$  dynamics.

To achieve this, we implement a simple control protocol in computer simulations. At each moment,  $\phi$  is chosen to minimize the magnitude of the vector  $(F_{\chi}, F_{\Pi})$ . That is, the cost function for the control protocol is given by

$$\phi_{\text{adapt}} : \text{Min}[\vec{F}_{\phi} \cdot \vec{F}_0]. \quad (25)$$

Since the minimization is a static function of the spread variables, the corresponding vector fields for  $\vec{F}_{\phi}$  for this control protocol can be calculated independently of the particular dynamics, and they are shown in Fig. 2(d). Here, we can clearly see the distinct tendency of  $\vec{F}_{\phi=\phi_{\text{adapt}}}$  to push the dynamics outward in  $\chi, \Pi$  space, compared to the fixed angle situations in Figs. 2(a) and 2(b). Before presenting the results of simulations of the effect of adaptive control on the system energy, we also define the useful quantities

$$E = \frac{1}{2}p^2 + \frac{1}{2}\Pi^2 + U_1 + U_2 + U_{12}, \quad (26a)$$

$$E_c = \frac{1}{2}p^2 + U_1, \quad (26b)$$

$$E_q = \frac{1}{2}\Pi^2 + U_2 + U_{12}. \quad (26c)$$

Here  $E$  is defined to be the system energy, which is the same as  $H$  in Eq. (21) except for the driving term.  $E_q$  is the sum of all  $\chi$ - and  $\Pi$ -dependent terms, which will not exist in the classical case, while  $E_c$  is the “classical” energy and thus satisfies  $E_c = E - E_q$ . Our analysis based on Fig. 2 predicts that  $E_q$  will be amplified by our adaptive measurement protocol (by increasing energy flow to  $U_{12}$ ) and we are interested in the change in the dynamics induced by this energy enhancement. It is also useful to define the time-dependent mean and

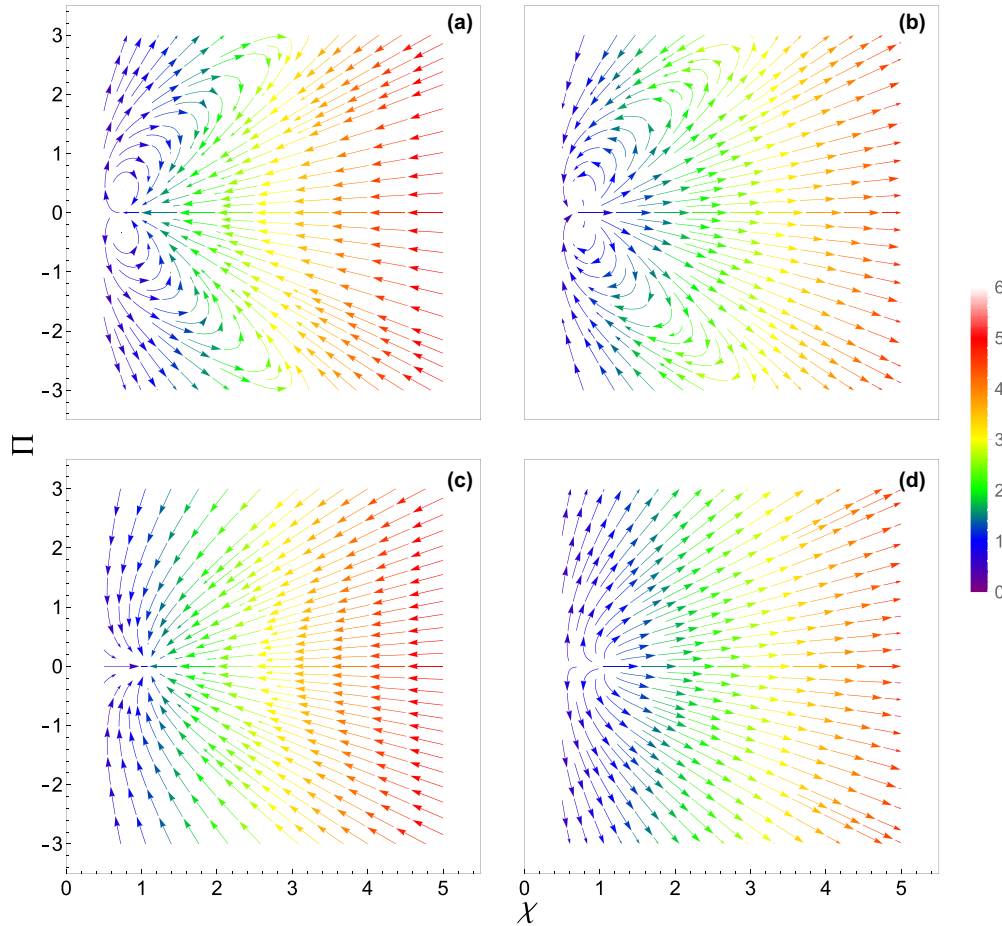


FIG. 2. Components of the dissipative force  $\vec{F} = \vec{F}_0 + \vec{F}_c \cos 2\phi + \vec{F}_s \sin 2\phi$ , resulting from the measurement as a function of LO phase-angle  $\phi$ , are shown for fixed  $\phi$  [(a)  $F_{\phi=0}$  and (b)  $F_{\phi=\pi/2}$ ] as well as the adaptive scheme discussed in the text [(c)  $F_0$  and (d)  $F_{\phi=\phi_{\text{adapt}}}$ ]. The color represents the strength of the field, which increases from left to right in this case. Notice that the inward-pointing force at fixed  $\phi = 0$  points somewhat outward at  $\phi = \pi/2$  and significantly more so with the adaptive scheme. All quantities plotted are dimensionless.

standard deviations of the various energy quantities in terms of a generic quantity  $X$  as

$$\bar{X} = \frac{1}{T} \int_0^T X dt, \quad (27a)$$

$$\Delta X = \frac{1}{T} \int_0^T \sqrt{(X - \bar{X})^2} dt, \quad (27b)$$

where, for example,  $\bar{E}$  represents the time average energy and  $\Delta E$  reflects the fluctuation of  $E$  along the time evolution. We now turn to some of the simulation results obtained to support our analysis. In addition to implementing the adaptive control methods presented here, we also study two fixed angle systems, using two particular parameter regimes where the dynamics were previously seen [10,12] to be especially sensitive to the measurement angle.

#### IV. RESULTS

We have studied a variety of parameter regimes as a function of  $\phi$ . We have demonstrated  $\phi$ -dependent dynamics, including transitions from regular to chaotic behavior. However, when explored for various  $\beta, \Gamma$  values, it is the change in energy throughput in the spread variables channel

that completely accounts for all the results seen and also those previously reported [10,12,13]. That is, changes in behavior due to the LO angle result from the change in the energy available, and in particular from the change in the quantum-classical coupling energy  $U_{12}$ , which naturally changes the potential energy landscape explored by the dynamics. Here we present two illustrative cases, where the coupling to the environment (the “classical dissipation”) is set at  $\Gamma = 0.10$  and  $0.08$ . For most choices of  $\Gamma$ , classically there is a single global attractor in the system. This holds true for the first case with  $\Gamma = 0.10$ , where there is a global chaotic attractor. However, the second example with  $\Gamma = 0.08$  is an edge case in which there is *not* a single global attractor in the classical system; instead, the system can go to a periodic *or* a chaotic attractor depending on the initial conditions. These classically coexisting attractors also appear in the semiclassical regime. This is a remarkable phenomenon not previously visible in quantum chaotic situations.

We start by revisiting fixed phase measurement results, preliminarily reported in Ref. [10]. Figure 3 shows the results of simulation of a single  $x$ - $p$  and  $\chi$ - $\Pi$  trajectory at  $\beta = 0.01$  and  $\Gamma = 0.10$ . We compare the results between  $\phi = 0$  and  $\phi = \pi/2$  without any adaptive change of the measurement phase. As predicted by the dissipation force analysis (Fig. 2),

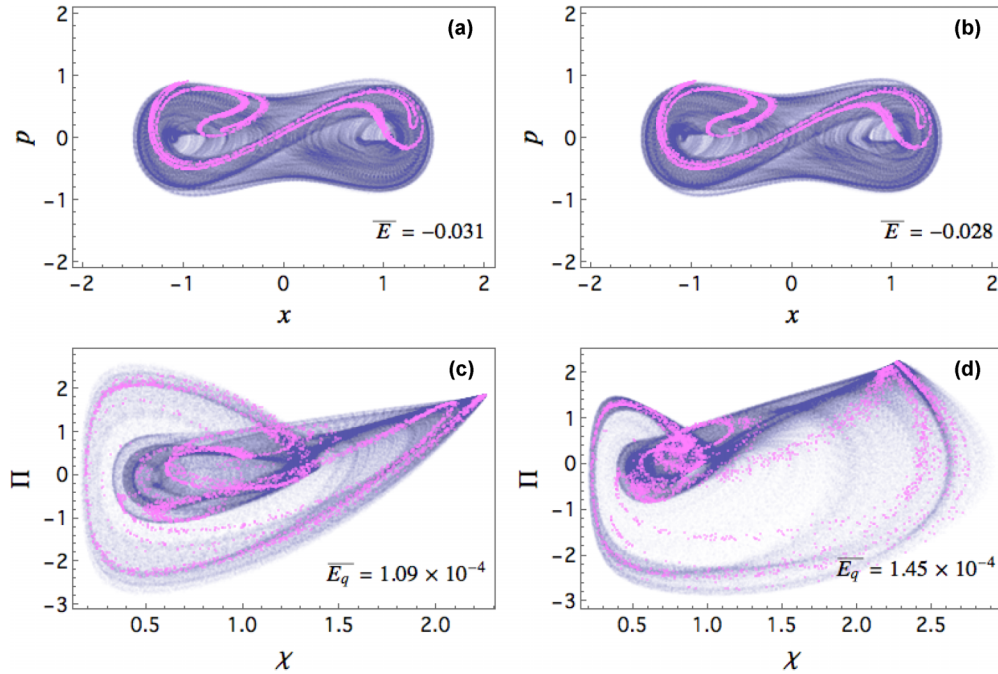


FIG. 3. Phase diagrams and Poincaré sections for (a) the  $x, p$  centroid subspace and (c) the  $\chi, \Pi$  spread subspace for a local oscillator angle  $\phi = 0$ , where  $\beta = 0.01$ ,  $\Gamma = 0.10$ . In (b) and (d) we see the same two figures for  $\phi = \pi/2$ . Notice a change in the “quantum” range, although the overall dynamics are not significantly affected. All quantities plotted are dimensionless.

the  $\phi = \pi/2$  case allows a larger range of  $\chi$  compared to the  $\phi = 0$  case. This correlates as predicted with an amplified range for  $\overline{E}_q$  achieved by increasing energy flow to  $U_{12}$ . Although measurement at  $\phi = \pi/2$  induces a substantial change for the  $\chi$ - $\Pi$  trajectory, neither the  $x$ - $p$  dynamics nor the time-averaged total energy  $\overline{E}$  are greatly affected. In this relatively classical regime ( $\beta = 0.01$ ), the total quantum effect introduced by the spread variables remains small.

With this baseline, we implement the adaptive measurement described by Eq. (25) at this same damping  $\Gamma = 0.10$ , while varying  $\beta$ . Even when the dynamics do not qualitatively change, there is a quantitative change in energy, and again the primary mechanism for effecting dynamical changes and the most dramatic effects of the measurement protocol can be summarized through the behavior of the energy terms. As such, in Fig. 4(a) we show the long-time average total energy  $\overline{E}$  of systems undergoing different measurement schemes over the range  $\beta = 0.005$ – $0.05$ . We see quite clearly that the adaptive measurement induces the largest change in energy compared with the other measurement schemes simulated. A similar trend is also observed in Fig. 4(b) for  $\Delta E$ , the standard deviation of  $H$ . The behavior of  $\overline{U}_{12}$  and  $\Delta U_{12}$  in Figs. 4(c) and 4(d) shows that the adaptive measurement protocol does amplify  $U_{12}$  tremendously as a channel to absorb energy from the driving and thus to alter the overall dynamics, as predicted by our control protocol.

An example of one of the most interesting changes induced by the adaptive measurement occurs at  $\Gamma = 0.08$ , where we are using a generic  $\beta = 0.01$  for discussion. The central features are captured in Figs. 5(c) and 5(d). Here we see that the adaptive control of  $\phi$  [Fig. 5(d)] has significantly expanded the  $\chi$ - $\Pi$  oscillator, so the range of  $\chi$  can be at 20-fold that of the  $\phi = 0$  case [Fig. 5(c)]. However, what is even more

remarkable is that this effect is not just visible in the spread dynamics. From Figs. 5(a) to 5(b), we see a big change in the  $x$ - $p$  dynamics as well: here the chaotic trajectory for  $\phi = 0$  in (a) becomes a chaotic transient that stabilizes to a periodic orbit for  $\phi = \phi_{\text{adapt}}$  in (b). The mechanism, which we explore more below, is that increased energy in the  $(\chi, \Pi)$  variables allows the  $x$ - $p$  dynamics to access larger  $x$ - $p$  values, which are then stabilized by energy absorbed by the drive  $(g/\beta) \cos \omega t$ . Notice that the total energy has increased as a result, so it is not merely a question of the energy in the spread variables being transferred to the centroid variables, but an actual change to a new, higher-energy steady-state. We dig deeper to try to clarify this novel phenomenon and its mechanism further by considering the time-dependent energy dynamics more explicitly.

In Figs. 6(a) and 6(c), we see that the adaptive measurement protocol results in the same behavior as in Fig. 5, although here the control protocol is turned on at  $t = 7000$ . After the adaptive measurement is turned on, we see that both  $\chi$  [Fig. 6(a)] and  $E_q$  [Fig. 6(c)] are amplified simultaneously, as explained in our previous analysis. Then, at around  $t = 11,500$ , the total energy  $E$  transitions sharply to a higher-energy regime, while  $\chi$  shrinks to a much smaller range [Fig. 6(a)]. Simulations confirm that this occurs simultaneously with the  $x$ - $p$  trajectory switching from the chaotic to the regular attractor. Although not shown here, details of this process can be seen in the Supplemental Material video about the phase-space evolution of the central and spread variables during the energy transition [35]: As the spread energy  $U_{12}$  fluctuates around a high value and  $\chi$  occasionally fluctuates to very high values, there comes a point where the centroid oscillator uses the extra energy in the spread dynamics to dynamically “tunnel” from the inner, chaotic attractor to the



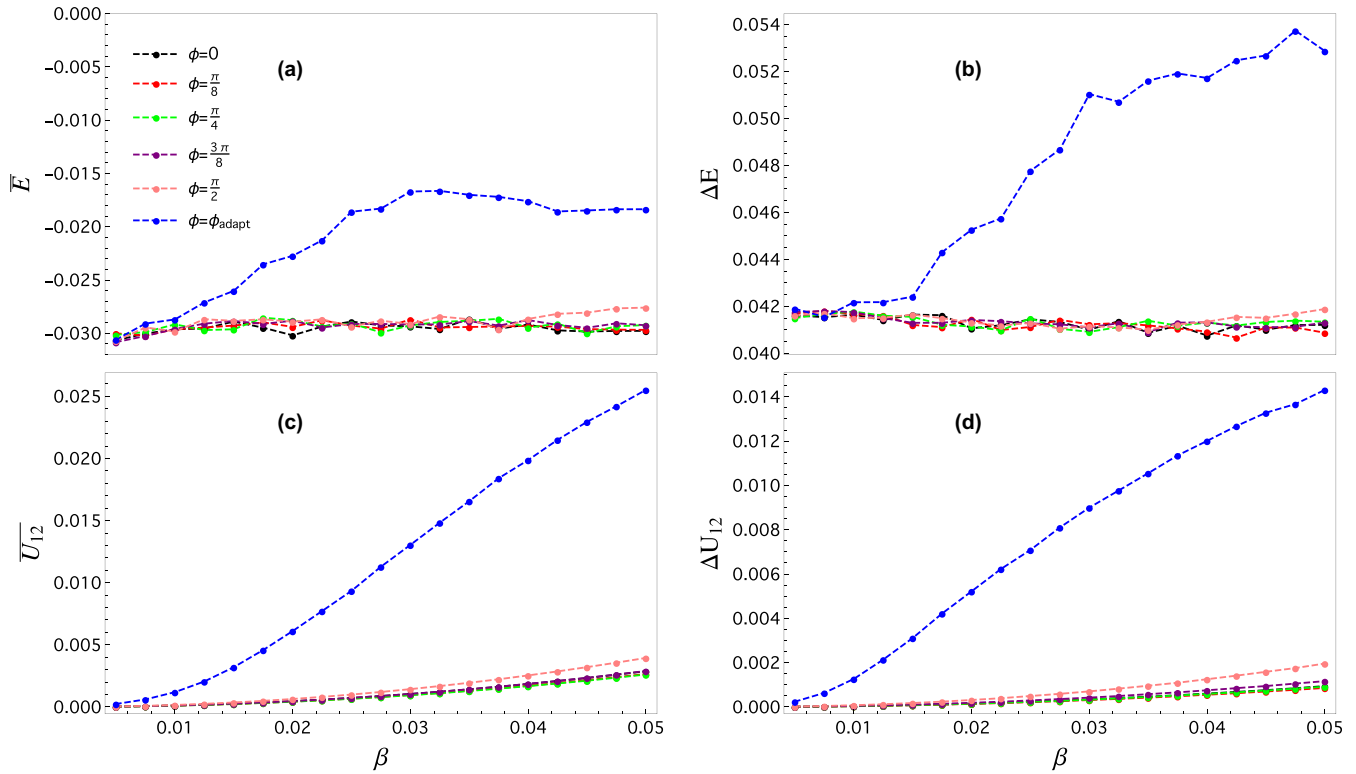


FIG. 4. Long-time averages of the system’s (a) total energy  $E$ , (b) quantum-classical coupling energy  $U_{12}$ , and (c),(d) their respective variances as a function of length scales  $\beta$ , for different measurement settings  $\phi$ , including the adaptive setting  $\phi = \phi_{\text{adapt}}$ . The adaptive setting (top blue line) increases the energy channeled through the spread variables—and, consequently, the “quantumness” as signaled by  $U_{12}$ —significantly more than just increasing  $\beta$  does for any fixed-angle measurement protocol. All quantities plotted are dimensionless.

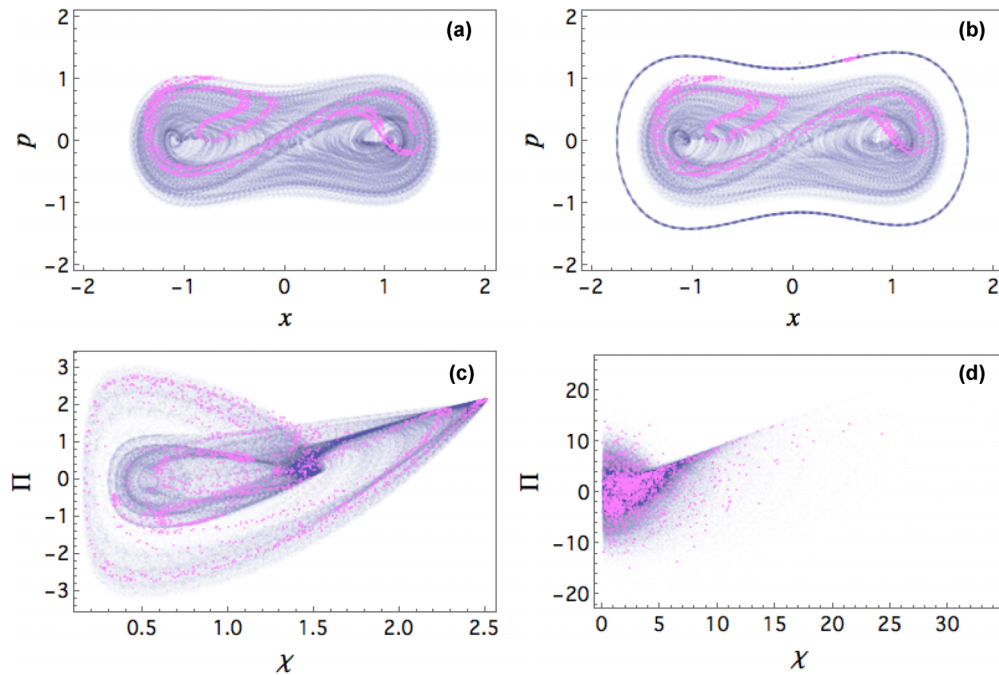


FIG. 5. Phase diagrams (purple lines of trajectories) and Poincaré sections (pink dots, representing these same trajectories sampled every drive period) for the  $x, p$  centroid subspace (a) and the  $\chi, \Pi$  spread subspace (c) for a fixed angle  $\phi = 0$ , compared to the adaptive control in (b) and (d). Notice the remarkable increase in the range of the  $\chi$ - $\Pi$  orbit and the dramatic appearance of a regular orbit in the  $x$ - $p$  space. This dynamical shift corresponds to the transition to higher  $\overline{E}$  and  $\overline{U}_{12}$  that occurs in the adaptive control scheme, as depicted in Fig. 4. Importantly, note that the chaotic behavior observed in (b) is transient; the dynamics stabilizes to the regular orbit after a finite period of time. All quantities plotted are dimensionless.

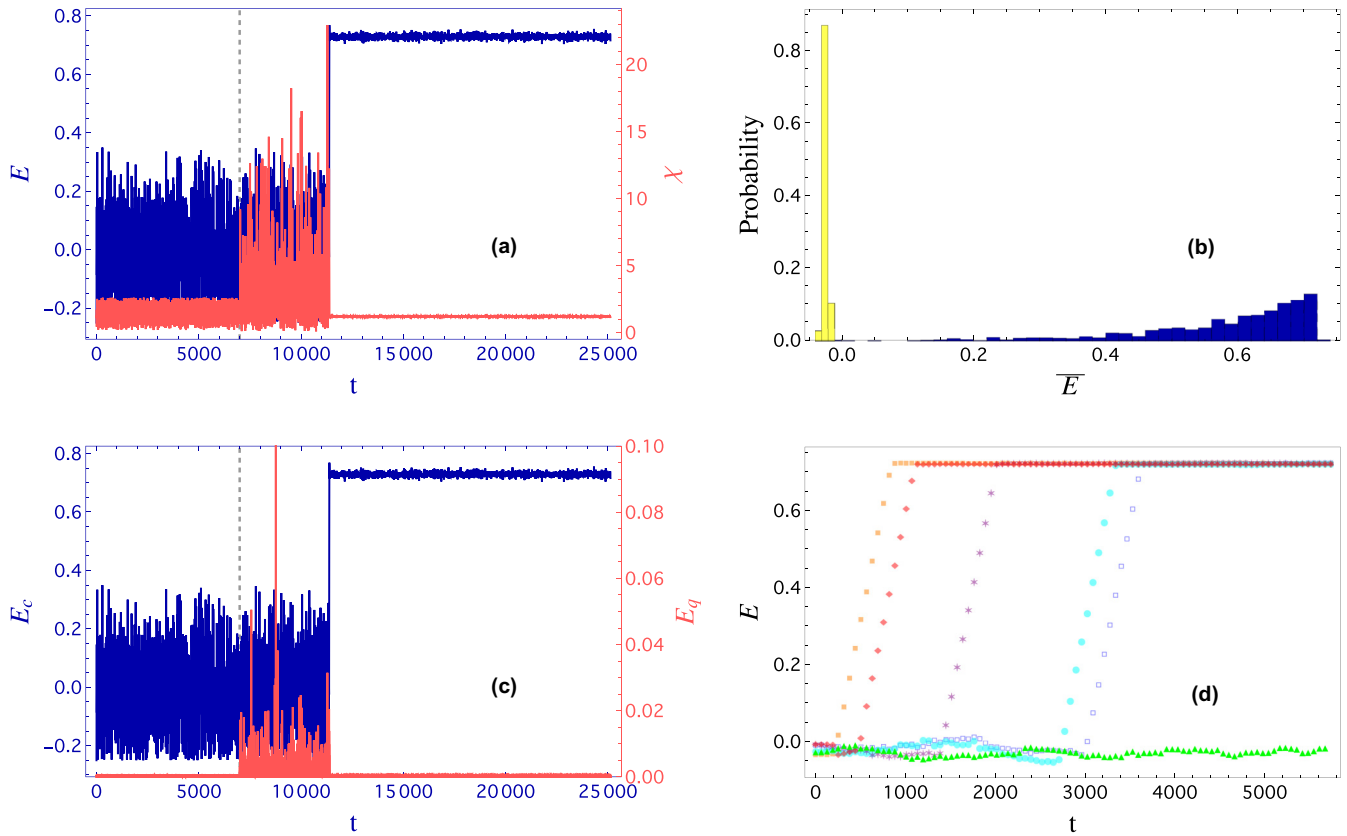


FIG. 6. Analysis of the energy dynamics. Parts (a) and (c) display  $E$ ,  $E_q$ ,  $E_c$ , and  $\chi$  as a function of time. The gray dashed vertical line at  $t = 7000$  indicates the time when  $\phi = 0$  is changed to  $\phi = \phi_{\text{adapt}}$ . A sudden jump appears at around  $t = 11\,200$  for  $E$ ,  $E_c$  (darker, blue) and  $\chi$ ,  $E_q$  (lighter, red). Part (b) shows the distribution of  $\bar{E}$  for  $\phi = 0$  (lighter, yellow) and  $\phi = \phi_{\text{adapt}}$  (darker, blue). 500 trajectories are simulated for each case. The  $\phi_{\text{adapt}}$  case is clearly centered at a high  $\bar{E}$  regime. Part (d) shows the moving average of  $E$  as a function of time with  $\phi = \phi_{\text{adapt}}$  for different trajectories, with time window  $\Delta t = 1000$  compared with the lowest curve (green triangles) at the  $\phi = 0$  case. Each trajectory's energy jumps at a different time, which explains the spread of the  $\bar{E}$  in (b). All quantities plotted are dimensionless.

outer, regular attractor. We note two features about Fig. 6(c): first,  $E_c$  leaps at the transition point considerably more than  $E_q$  shrinks (which we term dynamical tunneling); and second,  $E_q$  does not grow again even if the adaptive control is left on. This latter is attributable to the fact that in chaotic regimes, an ellipsoid of trajectories (the wave packet in this case) tends to spread. While this is normally kept in check by the dissipation, we were able to override this effect with the adaptive control. In contrast, in regular regimes, an ellipsoid of trajectories tends to focus, and in this particular case the adaptive control does not override this combination of dynamical focusing and dissipation.

In Fig. 6(d) we see moving averages of the total energy (with a time window of  $\Delta t = 1000$ ) for different individual trajectories in this coexisting attractor regime with the control turned on at  $t = 0$ , compared with the  $\phi = 0$  energy case shown in green. We observe that the energy leap for  $\phi = \phi_{\text{adapt}}$  happens at different times (this randomness is why this is like dynamical tunneling), even though each trajectory converges to the same final energy value. Furthermore, Fig. 6(b) shows the histogram of  $\bar{E}$  for 500 trajectories for both the adaptive measurement case and the fixed measurement case of  $\phi = 0$  for a total time of  $t = 6000$ . It is not hard to see that for the  $\phi = 0$  case, the energy jump never happens such that the histogram centers at a low energy (around  $-0.25$ ) for this

specific time length. However, for the adaptive case, since the energy jump happens at different times, the histogram of the time-averaged energy is more spread out and peaks in the high-energy regime (around  $\bar{E} = 0.7$ ). Thus we see that in this case, appropriate dynamical phase-setting on the LO significantly alters energy absorption through the quantum spread variables channel, and that this “quantum” energy—while not itself sufficient to maintain the resulting high-energy orbit—is the key factor in creating a dynamical transition in the centroid variables.

## V. CONCLUSIONS

To summarize the highlights, we have shown that for a driven nonlinear quantum oscillator, it is possible to understand the backaction induced by measurement as generalized noise and dissipation. Although arguably a general effect, our semiclassical analysis makes it clear that of the angle-dependent measurement backaction forces, noise effects act on the centroid or “classical” variables while the dissipation acts on the “quantum” spread variables. By focusing on the effect on these dissipation and noise forces of changing the phase angle for a LO used for homodyne measurement, we show that it is possible to alter the energy dynamics of the system such that the quantum spread variables act as an alternate

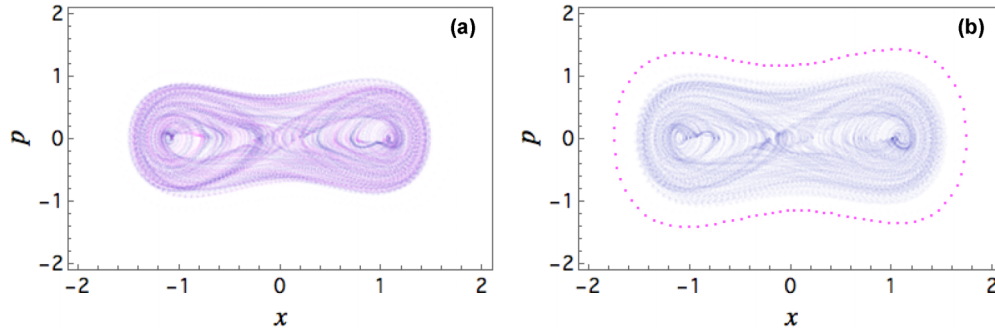


FIG. 7. The classical Duffing oscillator phase space plot. Trajectories with two kinds of initial conditions are plotted:  $(x_0, p_0) = (1, 0)$  (darker, blue) and  $(x_0, p_0) = (1.5, 1)$  (lighter, pink) at two different values of  $\Gamma$ . (a)  $\Gamma = 0.1$ , (b)  $\Gamma = 0.08$ . We see that the resulting trajectories, indistinguishable in (a), separate out into an “inner” chaotic trajectory and an “outer” regular orbit. All quantities plotted are dimensionless.

energy channel to absorb energy in different ways. Among the examples of the kind of dynamical change that is possible to effect, we demonstrate an example of a control protocol where the energy in the spread variables helps the “classical” variables to tunnel from low-energy, chaotic dynamics to high-energy, regular dynamics. This mechanism of using the spread variables as an alternate energy channel suggests a varied range of novel quantum control phenomena, including the possibility of slightly more complex protocols that would allow the system to cycle between different steady-states and thus enable novel quantum energy absorption devices.

In this paper, we have also proposed a quantum optical system where such effects might be seen. The proposed system serves as a proof of principle that our Hamiltonian, the quantum Duffing oscillator, is physically realizable, and our analysis shows that measurement backaction can be used to change the system state in interesting ways. However, modifications must be made before these correspond to actual experimental predictions. Specifically, we have assumed zero loss measurements to simplify computations, clearly not viable with a real experiment. To account for loss, our results must be generalized by replacing the SSE with the corresponding SME, thus allowing for mixed states. Further, we have assumed instantaneous feedback control, but any real experiment must have a delay between the measurement and  $\phi$ -update. Finally, our analysis in terms of  $\chi$ - $\Pi$  variables would need to be translated to observables more directly measured in the laboratory. Future work will investigate the possibility of analogous measurement-based control in light of these experimental realities, as well as other applications of such quantum backaction effects for useful and novel quantum behavior, including altering the energy dynamics of Bose-Einstein condensates.

#### ACKNOWLEDGMENTS

Internal support from Carleton College, including computational support from Bruce Duffy, is gratefully acknowledged. Many discussions with Andre Carvalho and Jessica Eastman on earlier stages of this work were very helpful and are also gratefully acknowledged. We thank the anonymous referees for a careful reading of the manuscript and useful feedback.

#### APPENDIX A: CLASSICAL DUFFING OSCILLATOR PHASE-SPACE PLOT

Understanding the baseline classical dynamics is always helpful in understanding the semiclassical dynamics investigated. To this end, the phase-space plots for the classical Duffing oscillator are shown in Fig. 7, where we have used  $\Gamma = 0.1$  and  $0.08$ . In these figures, we have plotted trajectories for different initial conditions. It can be observed that at  $\Gamma = 0.1$ , the two initial conditions lead to the same chaotic attractor. However, at  $\Gamma = 0.08$  the two initial conditions lead to two coexisting attractors—one chaotic and one regular. As shown in Sec. IV, at  $\Gamma = 0.08$  the adaptively measured quantum oscillator is able to jump from the inner attractor to the surrounding one even with the same initial condition.

#### APPENDIX B: SEMICLASSICAL DYNAMICS UNDER MEASUREMENT

The semiclassical approximation we use amounts to assuming [11] that the wave function is sufficiently localized by the action of the environment such that it can be represented in position space over  $q$  by the minimum uncertainty squeezed Gaussian as

$$\psi(q) = (2\pi V_x)^{-\frac{1}{4}} \exp[i[A(q-x)^2 + p \cdot (q-x)]], \quad (\text{B1})$$

with the time-dependent quantities  $V_x, A, x, p$  defining the evolution of the state, where  $A$  is complex in general. This form of  $|\psi\rangle$  relates to operator expectation values as

$$x = \langle \hat{Q} \rangle, \quad (\text{B2})$$

$$p = \langle \hat{P} \rangle \quad (\text{B3})$$

for the centroid variables. Considering the spread variables defined via  $\Delta \hat{u} = \hat{u} - \langle \hat{u} \rangle$  for an arbitrary operator, we get that

$$V_x = \langle \Delta \hat{Q}^2 \rangle \quad (\text{B4})$$

and that

$$A = \frac{1}{4V_x} (i + V_{xp}), \quad (\text{B5})$$

where

$$V_{xp} = \langle \Delta \hat{Q} \Delta \hat{P} + \Delta \hat{P} \Delta \hat{Q} \rangle, \quad (\text{B6})$$

such that the wave-function evolution is completely defined by tracking these two centroid variables and the two spread

variables. For completeness, we note that the third second-order moment

$$V_p = \langle \Delta \hat{p}^2 \rangle \quad (\text{B7})$$

does not need to be independently tracked since this squeezed Gaussian maintains the minimum uncertainty relationship

$$V_p = \frac{\hbar^2 + V_{xp}^2}{4V_x} \quad (\text{B8})$$

for noncommuting variables. We note for use below that higher moments for Gaussians are given by

$$\langle \Delta \hat{Q}^{2m} \rangle = \frac{(2m)! V_x^m}{m! 2^m} \quad (\text{no sum}), \quad (\text{B9})$$

$$\langle \Delta \hat{Q}^{2m+1} \rangle = 0. \quad (\text{B10})$$

To derive dynamical equations for the characteristics of the wave function just defined, we start with no environmental coupling (i.e., with  $\Gamma = 0$ , whence no Lindblad term) and show how a coupled classical oscillator system may be defined for this approximation. When the wave function above is substituted in Schrodinger's equation, we get the coupled set of ordinary differential equations

$$\frac{dx}{dt} = p, \quad (\text{B11})$$

$$\frac{dp}{dt} = -U_1^{(1)}(x) + \sum_{m=1}^{\infty} \frac{V_x^m}{m! 2^m} U_1^{(2m+1)}(x), \quad (\text{B12})$$

$$\frac{dV_x}{dt} = V_{xp}, \quad (\text{B13})$$

$$\frac{dV_{xp}}{dt} = \frac{\hbar^2 + \alpha^2}{2V_x} - \sum_{m=1}^{\infty} \frac{V_x^m}{(m-1)! 2^{m-2}} U_1^{(2m)}(x) \dots \quad (\text{B14})$$

Here we have used an expansion for the potential energy operator

$$\langle U_1^{(1)}(\hat{Q}) \rangle = U_1^{(1)}(x) + \sum_{m=1}^{\infty} \frac{1}{m!} \langle \Delta \hat{Q}^m \rangle U_1^{(m+1)}(x), \quad (\text{B15})$$

where  $F^{(n)} = \partial^n F / \partial u^n |_{\hat{u}}$ . Notice that the centroid equations deviate from the classical force  $U_1^{(1)}(x)$  with odd-derivative terms that include all even-order moments of the Taylor expansion around the centroid, while the even derivative terms enter in the  $V_{xp}$  equation. These expansions are infinite and exact under the Gaussian approximation, but they yield finite series with the number of terms depending on the higher-order derivatives of the potential. The system is now reduced to the dynamics of  $x$ ,  $p$ ,  $V_x$ , and  $V_{xp}$ . If we introduce the change of variables  $V_x = \chi^2$  and  $V_{xp} = 2\chi\Pi$ , Eqs. (B11)–(B14) transform to

$$\frac{dx}{dt} = p, \quad (\text{B16})$$

$$\frac{dp}{dt} = -U_1^{(1)}(x) - \sum_{m=1}^{\infty} \frac{\chi^{2m}}{m! 2^m} U_1^{(2m+1)}(x), \quad (\text{B17})$$

$$\frac{d\chi}{dt} = \Pi, \quad (\text{B18})$$

$$\frac{d\Pi}{dt} = \frac{\hbar^2}{4\chi^3} - \sum_{m=1}^{\infty} \frac{\chi^{2m-1}}{(m-1)! 2^{m-1}} U_1^{(2m)}(x), \quad (\text{B19})$$

where we have used the relationships

$$\frac{d\chi}{dt} = \frac{1}{2\chi} \frac{dV_x}{dt}, \quad (\text{B20})$$

$$\frac{d\Pi}{dt} = \frac{1}{\chi} \left( \frac{dV_{xp}}{dt} - \frac{\Pi d\chi}{dt} \right). \quad (\text{B21})$$

Remarkably, these new variables form an explicit potential energy system as our approximation to the Hilbert space, now for the classical coupled oscillators represented by the centroid variables  $x$ ,  $p$  and the spread-related variables  $\chi$ ,  $\Pi$ , respectively, with associated Hamiltonian

$$H = \frac{p^2}{2} + \frac{\Pi^2}{2} + U(x, \chi), \quad (\text{B22})$$

$$U(x, \chi) = U_1(x) + \frac{\hbar^2}{8\chi^2} + \sum_{m=1}^{\infty} \frac{\chi^{2m}}{m! 2^m} U_1^{(2m)}(x) \quad (\text{B23})$$

exactly as in the main text but with the specific Duffing Hamiltonian.

In the presence of environmental coupling, the equations above generalize, and using Ito stochastic calculus we get the set of coupled stochastic differential equations,

$$\begin{aligned} dx &= pdt + \sqrt{\Gamma}(2V_{xp} \sin \phi + (2V_x - 1) \cos \phi) dW, \\ dp &= xdt - 2\Gamma pdt + \frac{g \cos(\omega t)}{\beta} dt - \beta^2(x^3 + 3xV_x) \\ &\quad + \sqrt{\Gamma}(2V_{xp} \cos \phi + (2V_x - 1) \sin \phi) dW, \\ dV_x &= 2V_{xp} dt + \frac{\Gamma}{2} ((4V_{xp} - 8V_{xp}V_x) \sin 2\phi \\ &\quad + (4V_{xp}^2 - 4V_x^2 + 4V_x - 1) \cos 2\phi \\ &\quad + (-4V_{xp}^2 - 4V_x^2 + 4V_x + 1)) dt, \\ dV_p &= (2V_{xp} - 6\beta^2 V_{xp}(x^2 + V_x)) dt \\ &\quad + \frac{\Gamma}{2} ((4V_{xp} - 8V_{xp}V_p) \sin 2\phi \\ &\quad + (-4V_{xp}^2 + 4V_p^2 - 4V_p + 1) \cos 2\phi \\ &\quad + (-4V_{xp}^2 - 4V_p^2 - 4V_p + 1)) dt, \\ dV_{xp} &= (V_p + V_x - 3\beta^2 V_x(x^2 + V_x)) dt \\ &\quad + \frac{\Gamma}{2} ((-4V_{xp}^2 - 4V_x V_p + 2V_x + 2V_p - 1) \sin 2\phi \\ &\quad + (4V_p V_{xp} - 4V_x V_{xp}) \cos 2\phi \\ &\quad + (-4V_p V_{xp} - 4V_x V_{xp})) dt. \end{aligned} \quad (\text{B24})$$

It is worth noting [34] that dissipation causes solutions to these equations to rapidly converge to the minimum uncertainty condition for the three spread variables above, even if that is not the initial condition, such that the uncertainty relationship imposed by the Gaussian approximation is self-consistently justified and is stable. Using this to eliminate  $V_p$ , and the same change of variables as above transforming  $(V_x, V_{xp}) \rightarrow (\chi, \Pi)$ , we get the equations presented in Eqs. (16a)–(16d). The numerical regime of validity of this semiclassical approximation—which holds true for sufficiently strong localization—has previously been shown by comparison with full quantum simulations [10,18] to be approximately the regime  $\beta < 0.01$  for our  $\Gamma$  range. It has also



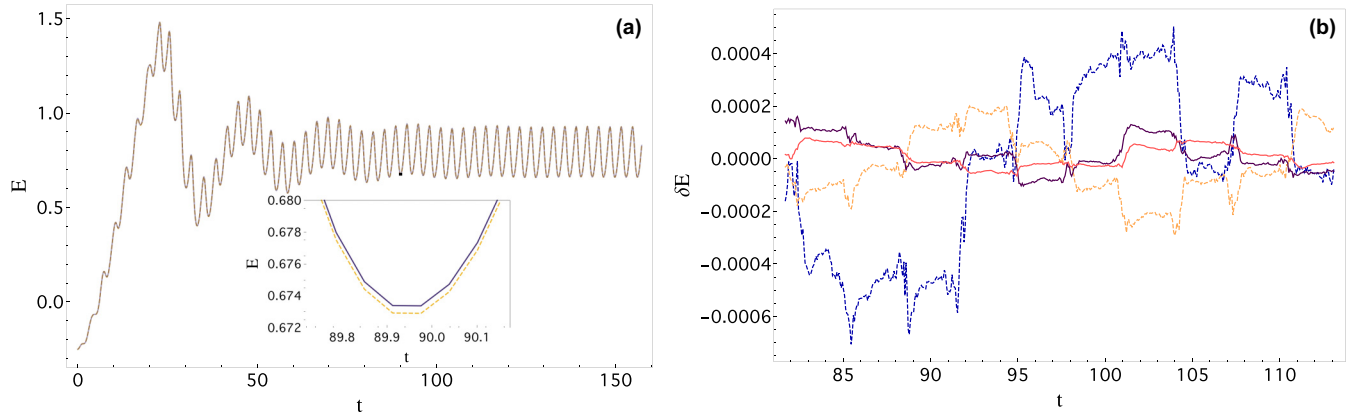


FIG. 8. (a)  $E$  averaged over 1000 trajectories for  $\phi = \frac{\pi}{2}$  (yellow, dashed) and  $\phi = 0$  (purple) at  $\Gamma = 0.05$  and  $\beta = 0.01$ . (b) The energy difference  $\Delta E$  between ensembles evolving at  $\phi = \frac{\pi}{2}$  and  $\phi = 0$  averaged over  $N$  trajectories; we see increasing convergence to (decreasing fluctuation around) 0 as  $N$  increases through  $1 \times 10^3$  (blue dashed),  $5 \times 10^3$  (orange dashed),  $2 \times 10^4$  (dark purple), and  $1 \times 10^5$  (light red). All quantities plotted are dimensionless.

been shown that qualitative results obtained from the semi-classical equations remain valid considerably deeper into the quantum regime of increasing  $\beta$ .

### APPENDIX C: BEHAVIOR OF THE ENSEMBLE ENERGY FOR DIFFERENT CHOICE OF $\phi$

One of the interesting features of the unraveling of stochastic Schrodinger equations into trajectories is that behavior visible in the conditioned trajectories (which are a specific realization of the “noise” implicit in quantum mechanics as

simulated by us corresponding to a measurement record in the laboratory) may not be visible in the density matrix dynamics. In particular, while the time-averaged energies for individual trajectories show  $\phi$  dependence (see Fig. 6), recovering the ensemble average at each moment in time of the dynamical variables  $x, p$  by averaging trajectories shows no such  $\phi$  effect. We verify this by calculating the evolution of  $E$  for different choices of  $\phi$  averaged over numerous trajectories. As shown in Fig. 8, the energy difference  $\delta E$  between  $\phi = \frac{\pi}{2}$  and  $\phi = 0$  reduces as the number of trajectories increases and tends toward zero. We note for completeness that time-averages of this energy difference would be even closer to 0.

- 
- [1] I. H. Deutsch, *PRX Quantum* **1**, 020101 (2020).  
 [2] M. S. Blok, C. Bonato, M. L. Markham, D. J. Twitchen, V. V. Dobrovitski, and R. Hanson, *Nat. Phys.* **10**, 189 (2014).  
 [3] S. S. Szigeti, A. R. R. Carvalho, J. G. Morley, and M. R. Hush, *Phys. Rev. Lett.* **113**, 020407 (2014).  
 [4] H. M. Wiseman, *Phys. Rev. Lett.* **75**, 4587 (1995).  
 [5] T. C. Ralph, A. P. Lund, and H. M. Wiseman, *J. Opt. B* **7**, S245 (2005).  
 [6] B. Higgins, D. Berry, S. Bartlett, H. Wiseman, and G. Pryde, *Nature (London)* **450**, 393 (2007).  
 [7] L. Martin, F. Motzoi, H. Li, M. Sarovar, and K. B. Whaley, *Phys. Rev. A* **92**, 062321 (2015).  
 [8] P. Campagne-Ibarcq, L. Bretheau, E. Flurin, A. Auffèves, F. Mallet, and B. Huard, *Phys. Rev. Lett.* **112**, 180402 (2014).  
 [9] Q. Li, A. Kapulkin, D. Anderson, S. M. Tan, and A. K. Pattanayak, *Phys. Scr.* **T151**, 014055 (2012).  
 [10] Y. Shi, S. Greenfield, J. K. Eastman, A. R. R. Carvalho, and A. K. Pattanayak, in *Proceedings of the 5th International Conference on Applications in Nonlinear Dynamics*, edited by V. In, P. Longhini, and A. Palacios (Springer International Publishing, Cham, 2019), pp. 72–83.  
 [11] A. K. Pattanayak and W. C. Schieve, *Phys. Rev. E* **50**, 3601 (1994).  
 [12] J. K. Eastman, J. J. Hope, and A. R. Carvalho, *Sci. Rep.* **7**, 44684 (2017).  
 [13] J. K. Eastman, S. S. Szigeti, J. J. Hope, and A. R. R. Carvalho, *Phys. Rev. A* **99**, 012111 (2019).  
 [14] I. Percival, *Quantum State Diffusion* (Cambridge University Press, Cambridge, UK, 1998).  
 [15] T. A. Brun, I. C. Percival, and R. Schack, *J. Phys. A* **29**, 2077 (1996).  
 [16] A. Kapulkin and A. K. Pattanayak, *Phys. Rev. Lett.* **101**, 074101 (2008).  
 [17] Y. Ota and I. Ohba, *Phys. Rev. E* **71**, 015201(R) (2005).  
 [18] B. Pokharel, M. Z. R. Mislion, W. Lynn, P. Duggins, K. Hallman, D. Anderson, A. Kapulkin, and A. K. Pattanayak, *Sci. Rep.* **8**, 2108 (2018).  
 [19] V. Gorini, A. Kossakowski, and E. C. G. Sudarshan, *J. Math. Phys.* **17**, 821 (1976).  
 [20] G. Lindblad, *Math. Phys.* **48**, 119 (1976).  
 [21] H. M. Wiseman and L. Diósi, *Chem. Phys.* **268**, 91 (2001).  
 [22] M. Rigo and N. Gisin, *Quantum Semiclass. Opt.: J. Eur. Opt. Soc. Pt. B* **8**, 255 (1996).  
 [23] G. J. Milburn and C. A. Holmes, *Phys. Rev. A* **44**, 4704 (1991).  
 [24] P. D. Drummond and D. F. Walls, *J. Phys. A* **13**, 725 (1980).

- [25] A. Imamoglu, H. Schmidt, G. Woods, and M. Deutsch, *Phys. Rev. Lett.* **79**, 1467 (1997).
- [26] P. Alsing, G. J. Milburn, and D. F. Walls, *Phys. Rev. A* **37**, 2970 (1988).
- [27] M. H. Rubin, D. N. Klyshko, Y. H. Shih, and A. V. Sergienko, *Phys. Rev. A* **50**, 5122 (1994).
- [28] C. K. Hong and L. Mandel, *Phys. Rev. A* **31**, 2409 (1985).
- [29] D. Walls, *Nature (London)* **306**, 141 (1983).
- [30] K. W. Murch, S. J. Weber, C. Macklin, and I. Siddiqi, *Nature (London)* **502**, 211 (2013).
- [31] S. J. Weber, A. Chantasri, J. Dressel, A. N. Jordan, K. W. Murch, and I. Siddiqi, *Nature (London)* **511**, 570 (2014).
- [32] J. Halliwell and A. Zoupas, *Phys. Rev. D* **52**, 7294 (1995).
- [33] W. Verstraelen and M. Wouters, *Appl. Sci.* **8**, 1427 (2018).
- [34] A. D. Maris, B. Pokharel, S. G. Seshachallam, M. Z. R. Misplon, and A. K. Pattanayak, *Phys. Rev. E* (to be published).
- [35] See Supplemental Material at <http://link.aps.org/supplemental/10.1103/PhysRevA.103.052212> for a video about the phase-space evolution of the central and spread variables during the energy transition.